Environmental Fluid Mechanics (2025) 25:5
https://doi.org/10.1007/s10652-025-10019-3

ORIGINAL ARTICLE

High fidelity simulations of contaminant dispersion in an urban environment with comparison to magnetic resonance imaging measurements

Mark Owkes[1] · Ty Homan[2] · Michael Benson[3] · Andrew Banko[2]

Received: 6 March 2024 / Accepted: 1 November 2024 / Published online: 11 January 2025

Abstract

The dispersion of a contaminant in an urban environment has the potential to impact a large population of people. In this work, a complex urban canopy flow based on the Oklahoma City downtown business district circa 2003 is studied using Magnetic Resonance Imaging (MRI) and high-fidelity Large Eddy Simulations (LES). MRI is a novel experimental technique that can provide high-resolution measurements in four dimensions (three spatial and temporal) for lab scale models. The experiments and simulations use the same geometry and boundary conditions providing a one-to-one comparison of the two methods. Results are presented on the time-averaged velocity and concentration fields, the temporal dynamics of the concentration plumes for a transient release, and a novel Cloud Identification Algorithm that can separate plumes produced by periodic contaminant releases used for ensemble averaging over many releases. The MRI and LES datasets both include millions of measurement voxels and the comparisons highlight the complex 3D nature of the flow including strong vertical velocities in spanwise street canyons and flow acceleration in streamwise street canyons. The concentration fields are qualitatively similar albeit the LES shows larger dispersion. A quantitative analysis with performance measures compares the datasets pointwise and demonstrates that the two 3D datasets are similar with respect to many measures including a fractional bias of 0.02 (ideal=0.0), correlation coefficient of 0.87 (ideal = 1.0), and the fraction points within a factor of 2 is 0.98 (ideal = 1.0). Plume analysis compares the arrival and residence time of contaminant and is found to vary significantly with location within the urban environment with arrival times between 0 and 1.25 and differences within the contaminant cloud less than 10% at most locations.

✉ Mark Owkes
mark.owkes@montana.edu

[1] Mechanical & Industrial Engineering, Montana State University, PO Box 173800, Bozeman, MT 59717, USA

[2] Civil & Mechanical Engineering, United States Military Academy, West Point, 752 Thayer Road, West Point, NY 10996-1905, USA

[3] Collection Science & Engineering, Oak Ridge National Laboratory, 1 Bethel Valley Rd, Oak Ridge, TN 37831, USA

Article highlights

- The complex and spatially and temporally varying flow of a contaminant through an urban environment is studied using experiments and high-fidelity simulations.
- Regions around buildings with particularly high and low contaminant concentrations are observed due to the presence of vortices in spanwise street canyons and the entrainment of clean freestream fluid due to vertical flow behind buildings.
- The resultant data sets provide millions of measurement points and predictions that can be used to assess other models.

Keywords Large Eddy simulation · Oklahoma city · Street canyons · Pulsed injection

1 Introduction

Urban environments combine a large population with the potential for health hazards due to the airborne dispersion of pollutants and chemicals. For example, vehicle traffic and industrial processes can increase the concentrations of aerosols and small particulates which adversely impact the respiratory and cardiovascular health of residents [1]. Emergency preparedness in the event of an accidental or intentional release of harmful chemicals or biological agents is also a concern of local and federal agencies [2]. Urban planners and emergency response personnel rely on predictive models of flow and scalar transport through urban areas to understand dispersion characteristics, develop regulations, forecast scenarios, and respond in real-time.

Modeling the urban canopy is challenging due to the wide range of length and time scales, both in the heterogeneity of building sizes and arrangements, and in the characteristics of the turbulence produced by the urban canopy flow [1, 3]. Near-field dispersion over the street and neighborhood scale in particular has an important effect on contaminant concentrations within the immediate vicinity of a release point [4, 5]. Understanding the mechanisms of near-field dispersion is also important for modeling the large-scale extent of the plume as it evolves downstream. Initial plume spread is governed by a combination of turbulent dispersion due to eddies within the urban canopy sublayer and mean flow dispersion around buildings [6]. The latter can lead to non-intuitive dispersion characteristics such as cross-wind spread, effectively increasing the spatial extent of the release as seen by the far-field [7, 8]. Contaminant concentrations have also been observed to vary sharply across intersections [9] and become channeled within street canyons [10]. Vertical transport in the wakes of isolated tall buildings is another important mechanism for enhancing fluxes out of the urban canopy [11]. These types of observations have underscored the importance of developing fast-running, 'building-aware' models that explicitly resolve the local building geometry (c.f., [12–16]), as well as the application of high-fidelity simulations and experiments to investigate near-field interactions.

Large eddy simulation (LES) is used to provide high-fidelity, three-dimensional mean flow and turbulence statistics for urban canopy flows. LES employs fewer modeling assumptions than Reynolds-Averaged Navier–Stokes (RANS) simulations, and therefore incurs lower model form uncertainty, making it an attractive technique for fundamental physics studies and for reduced-order model development [17]. For example, Brown et al. [18] used LES to simulate the dispersion of a contaminant in an urban environment and

found very good comparisons with experimental results. Gousseau et al. [19] simulated near-field pollutant dispersion using a geometry based on downtown Montreal. Comparisons to dispersion around simple, isolated buildings identified common regions of counter-gradient transport mechanisms and the significance of mean flow dispersion on lateral and vertical transport. Akinlabi et al. [6] also concluded that mean flow dispersion can be comparable to turbulent dispersive effects using a formal spatial averaging procedure applied to their LES data. Letzel et al. [20] and Cai et al. [21] used LES to quantify the shear layer dynamics at the top of street canyons and found intermittent vertical turbulent fluxes. Similarly, Llaguno-Munitxa et al. [22] examined the influence of rooftop geometry on the street canyon flow using LES validated against experimental measurements. García-Sánchez et al. [17] performed LES of the downtown Oklahoma City business district, based on the Joint Urban 2003 (JU2003) field tests [23], to evaluate prediction differences between the high-fidelity simulations and RANS. Kurppa et al. [24] applied LES to understand air-quality hazards within realistic urban canopies. Many of these ideas depend on turbulent dispersion which has been the focus of a few LES studies, e.g., [25–27]. The above studies present a representative but not exhaustive list of the application of LES to urban canopy flow studies, and the reader is referred to additional studies and the references therein, including [28–31].

Despite the success of LES in exploring the fundamental physics of urban canopy flows, and for evaluating simplified transport and dispersion models, these simulations still require experimental validation. This is because most LES computations utilize grids that are too coarse to explicitly resolve the dissipative turbulence scales or boundary layers along building surfaces, and therefore require subgrid and wall models, respectively [32]. Additionally, the LES simulations often have uncertainties in inflow boundary conditions and often use simplifications of terrain, building facades, roofs, etc. Ideally, validation experiments can be used to identify and improve LES models. García-Sánchez et al. [17] reviewed five different LES studies that made comparisons to experimental field test data, and also conducted simulations of the JU2003 campaign as summarized above. Uncertainty in the LES results, as measured by discrepancies with experimental observations and formal uncertainty quantification obtained via an ensemble of simulations, revealed that inflow or boundary condition uncertainties accounted for a significant component of the observed differences. The sparsity of measurements for field tests were also cited as a challenge for validation.

Boundary conditions are inherently uncertain in field measurements due to the complexity of the incoming atmospheric boundary layer and the often limited meteorological data available. While variable atmospheric conditions are important for capturing the complete dynamics of dispersion, these uncertainties make it difficult to evaluate the performance of LES simulations. For this reason, researchers also rely on wind tunnel and water channel experimental data obtained using optical [33, 34] and probe-based techniques [22, 35, 36]. These studies provide valuable data on mean and turbulence statistics with well-controlled boundary conditions; however, measurements are limited to select planar and point-wise data due to limitations of physical and optical access within the urban canopy.

Recently, magnetic resonance imaging techniques have been applied to water channel studies of urban canopy flows to complement optical and probe-based techniques by providing the ensemble-averaged, three-dimensional (3D) velocity and concentration fields throughout urban canopy arrays [11, 37]. MRI methods provide a unique opportunity to explicitly evaluate high-fidelity LES predictions of mean flow dispersion for scale urban models with well-specified boundary conditions.

In this work, the near-field dispersion in an urban environment is studied by comparing an LES simulation to a four-dimensional (three spatial dimensions and one temporal dimension) data set measured with Magnetic Resonance Imaging (MRI). The MRI technique provides roughly 1.7 million measurements of contaminant concentration and velocity vectors at 12 times [37]. In addition to the detailed output, the data set also contains well-characterized boundary conditions to make a one-to-one comparison between simulations and experiments at millions of spatial locations in the domain feasible. The LES simulation of contaminant dispersion is performed with Simcenter STAR-CCM+ by Siemens. The simulation is conducted using a computational mesh with approximately 6.9 million grid cells. An incompressible solver is used to solve for the velocity field which advects the contaminant with standard turbulence models. The simulation uses the same geometry as the experiments and boundary conditions are provided from MRI measurements of the velocity at the inflow plane.

The two datasets provide a one-to-one comparison of the complex flow of a contaminant in an urban environment and (1) build confidence in the novel transient MRI measurement technique and (2) allow for interesting flow dynamics within the complex urban environment to be studied. This manuscript provides a description of the experimental and numerical methods, a comparison of temporally averaged quantities, transient results from the pulsed contaminant release, and results from a novel algorithm that is used to identify unique contaminant clouds from the periodic pulsed results.

2 Methods

2.1 Geometry and flow configuration

This section describes the geometry and setup used in both the experiment and simulations. The setup for this work consists of a 1:2206 scaled model of downtown Oklahoma City shown in Fig. 1a. This location has been the focus of many studies due to the large scale Joint Urban 2003 experiment conducted here [38] Many subsequent works have been performed including analysis of the contaminant statistics in a full-scale experiment [39], additional characterization in wind [40] and water [37, 41] tunnel experiments, comparisons with simulations [18], and models [42], to name a few. The scaled model is placed within a 2.2 m long water tunnel (see Fig. 3) that mimics the atmospheric flow through the urban environment. This water tunnel has been used for a number of studies of urban flows [11, 18, 37, 43]. The apparatus consists of a flow development section with diffusers, a contraction, and a roughness section, followed by the urban canopy model. The test section has a rectangular cross-section of 196 mm in width and 110 mm in height, which is designed to fit in the MRI system. By comparison, the Colcord Hotel depicted near the center of the domain in Fig. 1 is 20 mm tall at the model scale.

Although the water channel is a confined domain in contrast to the true atmospheric flow, the blockage area is approximately 4% in the vicinity of the Colcord Hotel and the intersection adjacent to the Westin. These streamwise locations are the primary regions used for comparison with the simulation results. Further downstream around the groupings of tall buildings, the blockage ratio increases to about 27%. However, this increase in the blockage area affects the flow only near the end of the experimental field of view, which is described below. This region is not a primary focus of the analysis and comparisons.

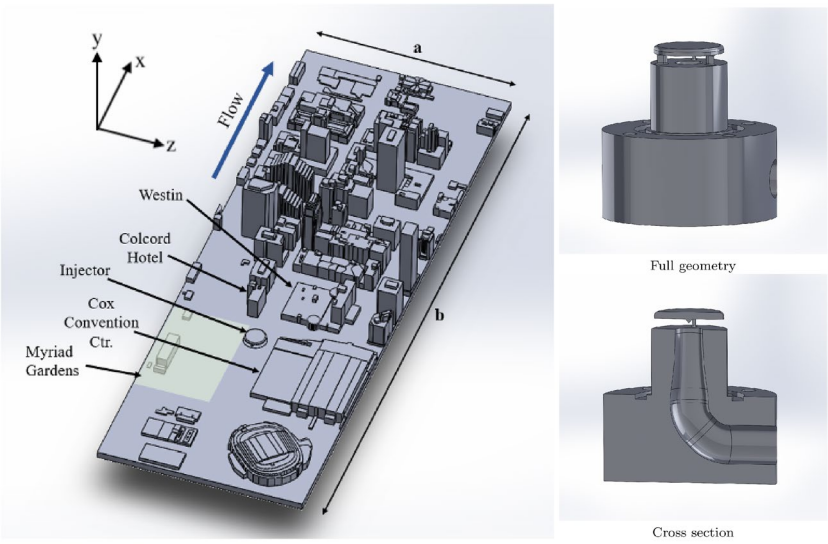

(a): Scaled model of Oklahoma City used in the study. The width of the test section a=196 mm, and the length b=567 mm.

(b): Closeup of the injector used to add contaminant to the flow.

Fig. 1 Urban environment geometry (**a**) and injector (**b**)

Additionally, the simulation framework will reproduce experimental no-slip boundary conditions on the side and top walls of the channel to enable a one-to-one comparison, including effects such as the blockage area.

Although the water channel is a confined domain in contrast to the true atmospheric flow, the blockage area is approximately 4% in the vicinity of the Colcord Hotel and the intersection adjacent to the Westin. These streamwise locations are the primary regions used for comparison with the simulation results. Further downstream around the groupings of tall buildings at the end of the experimental field of view, the blockage ratio increases to about 27%. This region is not a primary focus of the analysis and comparisons. While large, the effects of this blockage ratio are limited to the downstream end of the test section as supported by previous studies. In particular, Wang et al. [44], found that the impact of blockage on the flow upstream of where the blockage occurs is small. Additionally, a similar Oklahoma City geometry has previously been used in experiments on steady contaminant releases, and data were compared with simulations in an *unconfined* domain, which showed that the walls and blockage effects had little impact on the velocity field in the region of interest [45]. Finally, in this work, the simulation framework contains the walls and therefore will reproduce experimental no-slip boundary conditions on the sides and top of the channel to enable a one-to-one comparison, including any confinement effects such as the blockage area.

Water was used as the working fluid for both the experiment and simulation which mimics a neutrally-stratified boundary layer. The flow rate in the main channel was 390 ls per minute, which results in a bulk average velocity of 0.3 m/s. For reference, Fig. 2 plots the boundary layer profile obtained from the experiments near the end of the roughness section. The profile was averaged in the spanwise direction as described in [37]. A best fit of the logarithmic velocity profile with Karman constant $\kappa = 0.41$ estimates a friction velocity of $u^* = 0.042$ m/s and a roughness height of $z_0 = 0.7$ mm [46, 47]. Note that the

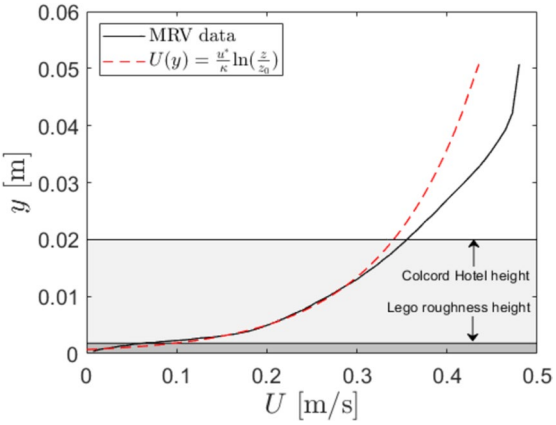

Fig. 2 Boundary layer profile at the end of the roughness section. A best fit of the logarithmic velocity profile estimates the friction velocity to be $u^* = 0.042$ m/s and the roughness height to be $z_0 = 0.7$ mm. The heights of the Colcord Hotel and the lego roughness elements are indicated for reference

velocity profile departs from the logarithmic behavior beginning at approximately the height of the Colcord Hotel. Using the viscosity of water at 20 °C and the lego roughness height of $h = 1.8$ mm, the dimensionless roughness element height in viscous units is $h^+ = u^* h/\nu = 75$. Similarly, the roughness Reynolds number is $Re^* = u^* z_0/\nu = 29$. Therefore, the upstream boundary layer is in the fully rough regime [47].

The building Reynolds number is defined as $\mathrm{Re}_H = UH/\nu = 6000$ for urban-like canopies, where U is the bulk velocity, H is the height of the Colcord Hotel, and ν is the kinematic viscosity of water at 20 °C. Alternatively, a velocity scale taken near the top of the Colcord Hotel would yield a similar Reynolds number magnitude as evidenced by the boundary layer profile in Fig. 2. This Reynolds number indicates that the flow will be fully turbulent and provides an approximation of the atmospheric flow through an urban environment because the large eddies responsible for the dispersion of the plume are represented. Previous studies have shown that results for flow and dispersion in the wake of a building are independent of Reynolds number when the Reynolds number exceeds a critical value. The critical value varies but has been found to be roughly 4000 to 11,000 and depends on the state of the upstream boundary layer [48–53]. For highly rough turbulent boundary layers and building heights less than the boundary layer thickness, similar to this experiment, [51] found that the critical Reynolds number is closer to 4000. The Reynolds number in this study is greater than this lower bound and of similar magnitude to the range of critical Reynolds numbers. While larger Reynolds numbers are typically desired to produce the widest spectrum of turbulence scales, the chosen flow conditions were selected due to a tradeoff between pumping capacity, compatibility of the test section size with the MRI diagnostics, increasing the Reynolds number by increasing the building heights, and minimizing the blockage ratio of the buildings within the channel.

The contaminant is released from an injector and the crossflow advects the contaminant through the urban environment. Details of the injector are shown in Fig. 1b. The contaminante enters through the inflow duct (bottom right), turns 90 degrees through the injector, and exits at the top where a horizontal circular plate redirects the contaminant momentum radially outward. The horizontal circular plate is held in place by three supports. The diameter of the injector tube where it meets the test section floor is 8 mm, and the circular plate is 20 mm in diameter and 3 mm above the test section floor. Therefore, the injector in the small-scale models is comparable to a low-level building structure. The simulation models

the full injector geometry in order to capture any near-field disturbances to the urban canopy flow.

The injection of contaminant is performed using a periodic or pulsed injection consisting of a 1-hertz cycle with roughly 0.4 s with the injection on followed by 0.6 s with the injection off. This periodic injection allows for computing flow statistics ensemble averaged over many injections. The measured injection flow rate from the experiment and a modified rate used in the simulations are shown in Fig. 4. The injection flow waveform is identical for the first 0.435 s. After this time the experimental flow rate shows a fluctuating flow with negative and positive velocities when the injection flow stops due to inductance within the inlet tubing. The simulation contaminant velocity was set to zero from $t = 0.435$ s through $t = 1s$ to avoid issues associated with a negative inflow velocity. While the experiment exhibits some oscillatory flow, the effect on the total volume of contaminant injected is negligible (c.f. [37]) additionally the transition time of 0.435 s was chosen such that the net flux of contaminant into the domain during each injection event is equal for both the experiment and simulation. The peak injector flow rate was 1 l per minute, which corresponds to an average radial outflow velocity of 0.08 m/s at the edge of the injector.

2.2 Experimental methods

The three-dimensional (3D), ensemble-averaged velocity and concentration fields were measured using magnetic resonance imaging (MRI) techniques as described in detail by Homan et al. [37], and a brief overview is provided herein. The main channel flow was supplied by two centrifugal pumps and controlled using a paddle wheel flow meter and diaphragm valves. The injection flow was supplied by a centrifugal pump and computer-controlled solenoid valve system to generate the pulsed injection waveform. The flow rate injection waveform was measured using an ultrasonic flow meter (Transonic Systems PXL flow probe). The flow was routed from large reservoirs, through the pumps, and to the channel using reinforced flexible tubing.

Data were acquired using a clinical grade 3 Tesla GE Signa Discovery 750 MRI system at the Richard M. Lucas Center for Imaging at Stanford University. Magnetic resonance velocimetry (MRV) and magnetic resonance concentration (MRC) measurements were performed using a phase-locked, three-dimensional phase contrast sequence [54]. The scan sequence was phase-locked to the injection waveform using a TTL signal routed through an ECG emulator which triggers the gating software of the MRI system. The Fourier-space image data were collected and sorted into six equally-spaced temporal phases over the injection cycle and then linearly interpolated in time to 12 temporal phases prior to applying the reconstruction algorithm to convert data into physical-space images. Therefore, the reconstructed temporal resolution was 1/12th of the injection cycle as indicated in Fig. 4. The spatial resolution was 1.5 mm in each direction covering a field of view that was 256 mm × 204.8 mm × 138 mm in the streamwise (x), vertical (y), and spanwise (z) dimensions, respectively. Note that the x, y, z coordinate system is shown in Fig. 1. This field of view encompasses the rectangular test section and external components such as the injector piece to prevent aliasing of the MRI signal from fluid regions outside of the field of view. The field of view is divided into measuremnt cubes refered to as voxels. The 1.5 mm voxel resolution corresponds to 3.3 m spatial resolution at full-scale. The choice of spatial and temporal resolutions was made to balance the fidelity of the data against the scan times needed to acquire the data. With these parameters, the MRV and MRC scans took approximately 6 and 12 h, respectively. Once the data are collected, several days are required to

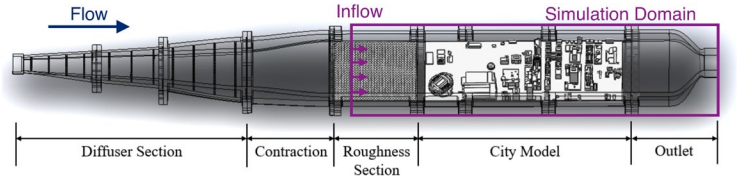

Fig. 3 Water tunnel used for the experimental measurements. Key dimensions include 238 mm for the length of the roughness section and 567 mm for the length of the city model. Additional dimensions and details of the water tunnel are included in [37]. The purple rectangle shows the portion of the experiment used in the simulations. The inflow boundary condition used in the simulation was measured experimentally

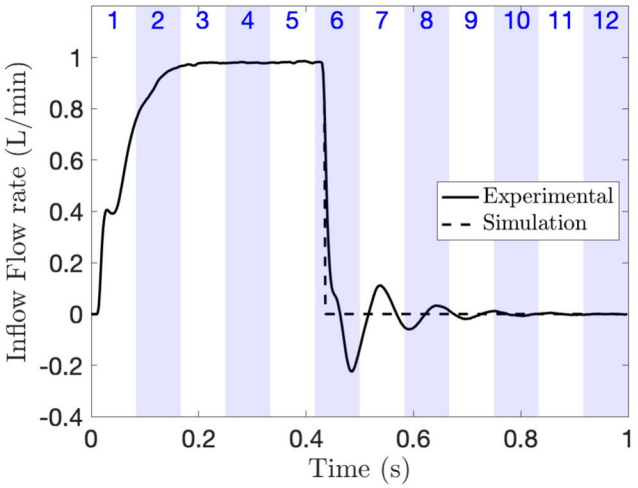

Fig. 4 Flow rate of contaminant injection measured in the experiment and used in the simulation. The blue colored bars with associated numbers indicate the 12 phases where the mean velocity and concentration data were computed

post-process the data, remove spurious vectors due to partial volume effects, and apply the concentration stitching technique combining multiple MRC scans as described in [55].

Velocity and concentration data were acquired in separate MRV and MRC scans. For the MRV, the velocity encoding values (VENCs), which determine the maximum measurable velocity, were set to 0.8 m/s in each direction. A 0.06 M solution of copper sulfate (CuSO4) was added to the water in order to enhance the signal-to-noise ratio. This concentration of CuSO4 has a negligible effect on the fluid properties. A series of alternating scans with the flow on and flow off were conducted. These scans were averaged and the flow off scans were subtracted from the flow on scans to correct for imaging artifacts due to eddy currents. Additional details of the MRV technique can be found in [56] and [37]. The average uncertainty in each velocity component over the field of view was calculated to be 0.0169 m/s, or 5.4% of the bulk velocity in the channel. However, the local uncertainty for different voxels varies based on the local velocity magnitude and turbulence level. Therefore, the average relative uncertainty computed over the field of view, excluding regions with near zero velocity, is approximately 4.3 % of the local velocity magnitude. Further

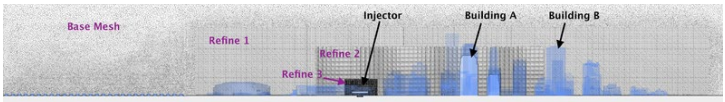

Fig. 5 Computational mesh, shown in black, on a plane through the middle of the urban environment. The mesh contains the base size and three refinement zones each with increased resolution. The locations are indicated by the labels. Buildings are shown in transparent blue. Labels on particular buildings are used when discussing the mesh resolution

restricting the region of interest to heights within the urban canopy yields an average relative uncertainty of 7.8% of the local velocity magnitude.

For the MRC scans, the same scan sequence was used with the VENCs set to 8 m/s such that the images are insensitive to fluid motion. MRC measures the concentration of the injected fluid by using the relationship between the image magnitude and the concentration of injected CuSO4 as a contrast agent. Specifically, image magnitude increases with increasing CuSO4 concentration, and the relationship is linear over a range of concentrations. The MRC technique requires data from multiple background, reference, and standard scans as described in [57] and [55]. Background scans consist of scans with water flowing through both the main channel and injector, reference scans flow a 0.02 M CuSO4 solution through the main channel and injector, and standard scans imaging the mixing between pure water in the main channel and 0.02 M CuSO4 solution in the injector. Repeated scans of each type are averaged together and combined to produce a concentration field that varies from zero in the main flow to unity in the injector. Additional scans injecting higher concentration CuSO4 solutions were also acquired and combined with the standard scans to reduce uncertainty within dilute regions of the plume as described in [55]. This resulted in a final experimental uncertainty that was 2.2% of the injected concentration within the dilute regions of the plume.

2.3 Simulation methods

The simulation is performed on the simulation domain shown in Fig. 3 using Simcenter STAR-CCM+ by Siemens. A WALE subgrid-scale turbulence model is used with the large-eddy simulation (LES) methodology. The contaminant is modeled as a passive scalar that is advected by the flow and disperses due to turbulence. The unresolved dispersion is modeled using a turbulence dispersion model with a subgrid-scale turbulent Schmidt number of 0.9. This is a standard set of turbulence models (defaults in STAR-CCM+) and provides a reference for how a standard LES simulation compares with the MRI experimental measurements. The timestep size was chosen to limit the convective Courant-Friedrichs-Lewy (CFL) number to be less than 1.

The computational mesh is shown in Fig. 5, which consists of 6.9 million polyhedral grid cells. The mesh resolution is the finest around the contaminant injector and gets progressively coarser moving away from the injector. Additionally, the mesh is further refined near solid boundaries by using two prism layers. The largest computational cells have a size of roughly 4 mm, however the largest computational cell size within the region of interest (MRI measurement region) is 1.2 mm, which is about the same size as the MRI measurement cells that have a size of 1.5 mm. The mesh resolution was determined after performing a mesh-independent study looking at the velocity and contaminant. Figure 6 shows the 5% isosurface of contaminant on coarse (1 million), medium (4 million), and

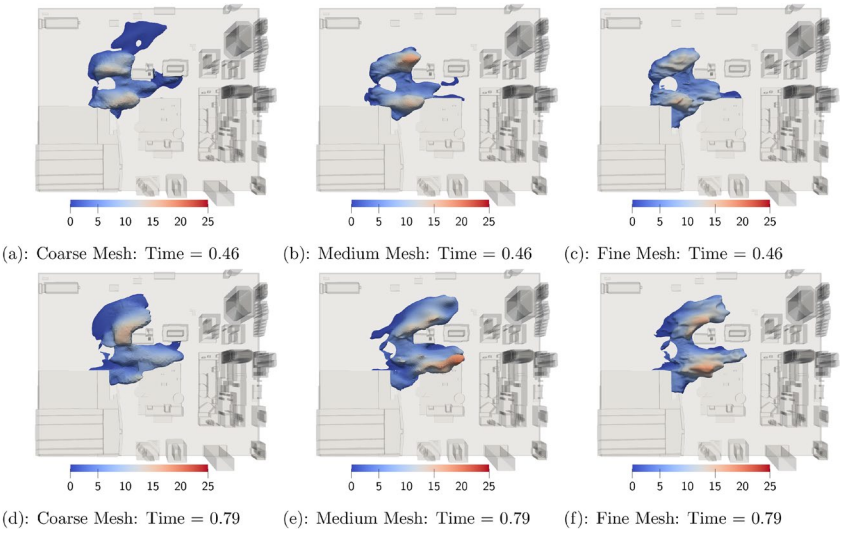

Fig. 6 Isosurfaces of contaminant colored by the vertical height (mm) of the isosurface. Results are shown on coarse (left), medium (center), and fine (right) computational meshes and at a time of 0.46 (top) and 0.79 (bottom). These times correspond with phases 6 and 10 of the contaminant injection (see Fig. 4)

fine (6.9 million) grids. For reference, the fine mesh has 50 grid cells across the diameter of the injector within the Refine 3 zone, 21 cells across Building A within the Refine 2 zone, and 13 cells across Building B within the Refine 1 zone, where these buildings and refinement zones are identified in Fig. 5. All the solutions have similar main features with the medium and fine being very similar. Note that the contaminant field depends on both the advection and dispersion of contaminant and convergence of this field assess that both the velocity and contaminant fields are mesh independent. These findings are similar to previous work that used simulations of the same water tunnel and observed mesh-independent results on a mesh with roughly 5 million cells [43].

Boundary conditions for the LES simulations include the streamwise velocity inflow (purple arrows in Fig. 3), contaminant inlet within the injector, outlet, and solid walls of the urban environment. For the streamwise velocity inflow, the time-averaged velocity was measured using MRI near the beginning of the roughness section on a two-dimensional, streamwise-normal plane covering the entire cross section (Fig. 3). This full mean velocity plane is used as the boundary condition in the LES simulations along with a 3% turbulence intensity. The low turbulence intensity is characteristic of the upstream flow conditioning. Placing the simulation inlet plane at the upstream end of the roughness section allows the turbulent LES boundary layer to naturally evolve over the roughness elements, consistent with the experiment. The top and side walls are smooth surfaces. All walls are modeled as no-slip boundaries with the bottom-wall roughness and the downstream buildings explicitly resolved, and the outlet is an outflow condition. The contaminant injection flow rate used in the LES is shown in Fig. 4 and is based on the experimental measurement. A uniform velocity profile is specified at the entrance to the injector (Fig. 4).

Simulation results are collected once the simulation reaches a stationary state. To achieve a stationary state in the crossflow, at least 10 flow-through times were simulated. The flow-through time is defined based on the mean streamwise velocity (0.3 m/s) and length of the simulation domain (1.1 m), which gives a flow-through time of 3.7 s.

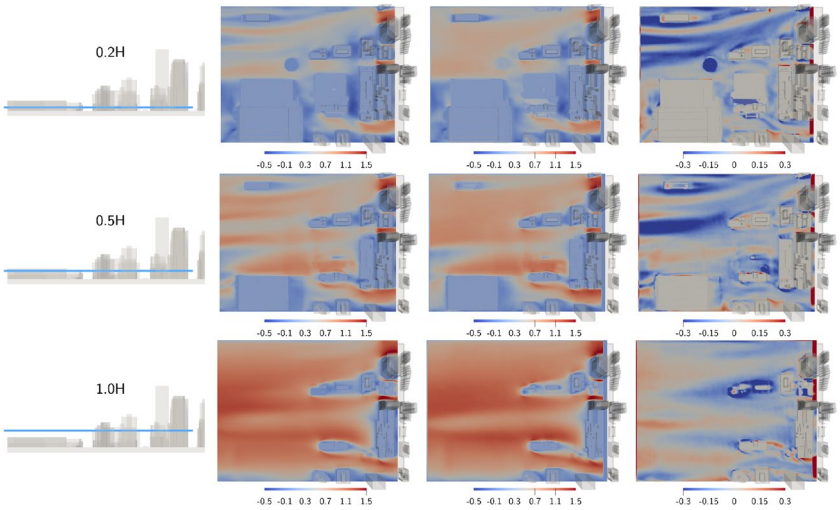

Fig. 7 Comparison of time-averaged streamwise velocity in (m/s) for LES (**b**) and MRI (**c**) and the difference between them (**d**). Results are organized by rows that vary the non-dimensional height of the cut plane. The height associated with each row is shown by the plane in the left column (**a**)

Therefore, simulations were run for at least 37 s before results were collected. This time to achieve a stationary state incorporates 37 contaminant injection events which are sufficient to remove any transient injection artifacts. Results are collected, in a method similar to the experiments, where the 1 hertz injection period is divided into 12 bins. Contaminant and velocity are time-averaged within each of these bins over at least 10 injection pulses (10 s).

The fine mesh is used to generate results in all the subsequent sections. With this mesh and the flow through times discussed above, the simulations required roughly one week on the Hyalite high-performance computing (HPC) resource at Montana State University which has 16 CPU Xeon CPU nodes.

3 Comparison of LES and MRI results

The simulation and MRI measurements provide four-dimensional datasets (three-spatial and time). These data-rich results are compared in this section. To allow for comparison, the LES dataset was interpolated to a grid that matches the MRI measurement cells.

3.1 Time-averaged velocity

The time-averaged velocity streamwise velocity (x-direction) is shown in Fig. 7. The results are shown at three heights described with the images in the left column. The heights are defined with-respect-to H, which is the height of the Colcord Hotel (Fig. 1). LES results have been cropped to the region of interest that includes the injector and some of the downstream buildings. This is the region where MRI measurements were taken. Overall, the LES and MRI agree very well and both capture the main characteristics of the flow. For

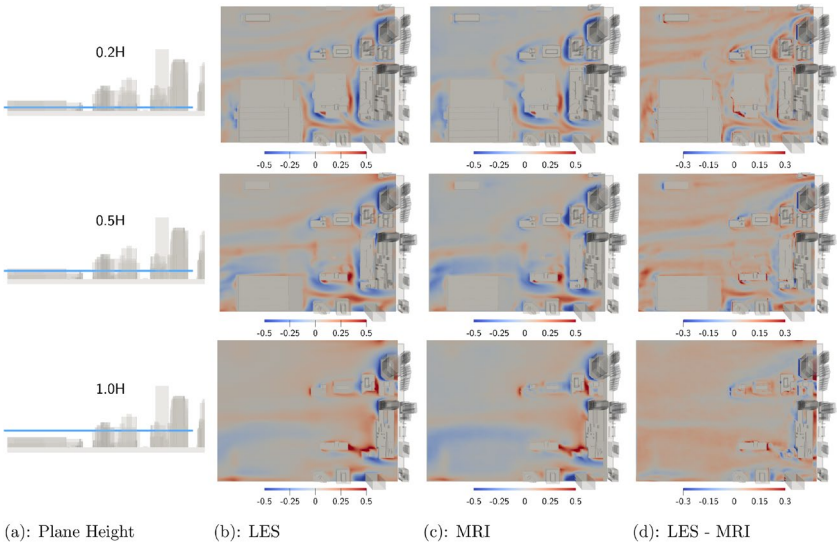

Fig. 8 Comparison of time-averaged vertical velocity in (m/s) for LES (**b**) and MRI (**c**) and the difference between them (**d**). Results are organized by rows that vary the non-dimensional height of the cut plane. The height associated with each row is shown by the plane in the left column (**a**)

example, the streamwise velocity is accelerated when passing between buildings and large velocities are present in both the LES and MRI results in the street canyons that are aligned with the flow. The magnitude of velocities is very similar at all heights and locations. The difference between the LES predictions and MRI measurements is shown in column (d). The largest difference appears at lower heights (0.2H and 0.5H), where the velocity entering the measurement domain is different in the LES simulations than in the MRI measurements. The LES predicts overall lower velocities at these heights and more variation in the spanwise direction (z-direction). This velocity difference will impact the contaminant transport which depends on the velocity. This could be a result of an error with the inflow boundary condition or challenges in resolving the boundary layer that develops over the roughness section.

The time-averaged vertical (y-direction) velocity is shown in Fig. 8. This velocity shows how the flow rises and falls due to the complex urban environment. In some spanwise street canyons, particularly those with taller buildings downstream, there is a large negative vertical velocity. This is due to the large buildings blocking the streamwise flow and causing acceleration in the vertical and spanwise directions. The difference between the LES predictions and MRI measurements is shown in column (d). The largest discrepancies occur where there are large gradients in vertical velocity near buildings.

Streamlines in the velocity field within some interesting areas of the flow are shown in Fig. 9. The lower set of streamlines (starting at a smaller z location) enters the measurement region from the crossflow and enters into the region between two medium-tall buildings. The flow swirls around in this street canyon before exiting over the top of the downstream building where it then enters the next space between two buildings and brings the fluid down into this region. The LES and MRI agree very well in the prediction and measurement of these phenomena. The upper set of streamlines enter a longer spanwise street canyon and swirl in a spanwise vortex before exiting down a streamwise street canyon. The

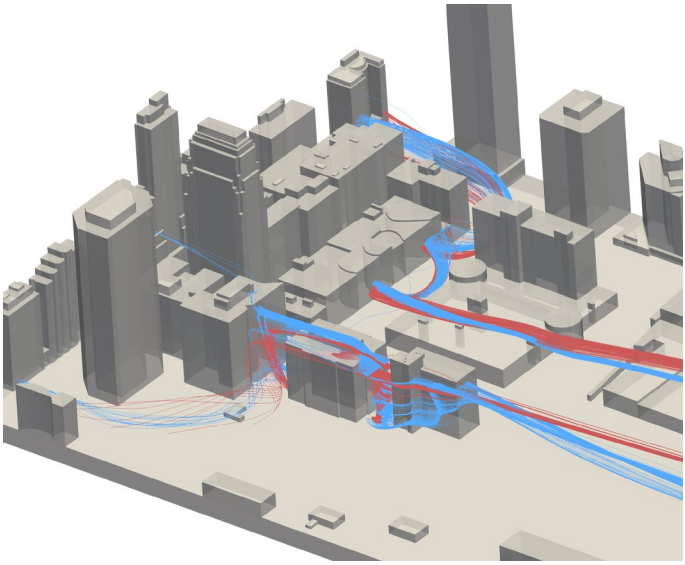

Fig. 9 Streamlines in the time-averaged LES (blue) and MRI (red) velocity fields

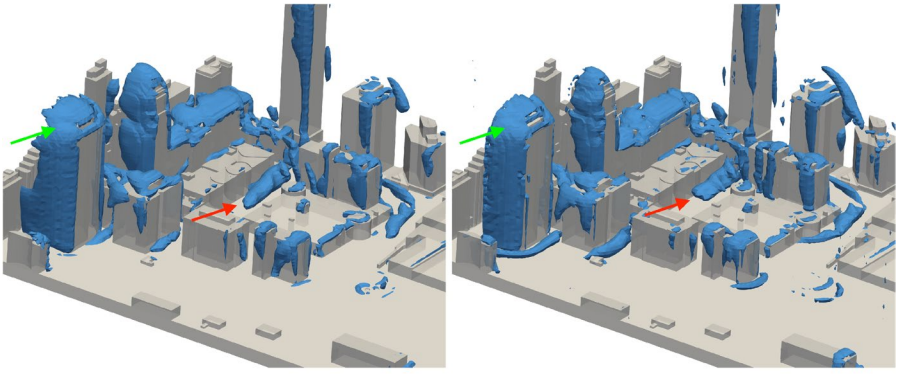

(a): LES (b): MRI

Fig. 10 Comparison of 0.005 isosurfaces of Q-criterion for LES (left) and MRI (right). The green arrow indicates a large vortex around the edges of a tall building. The red arrow indicates a prominent vortex in a spanwise street canyon

idea of the flow around nearby buildings has been investigated [58, 59], but this work provides insight into just how complex these flows can be in realistic urban environments. The reasonably good agreement seen between the LES and MRI results highlights how useful both of these techniques are in measuring or predicting these complex flows.

Isosurfaces of positive Q-criterion are a common method for identifying vortices in a turbulent flow [60]. Figure 10 compares the 0.005 isosurfaces of Q-criterion. Most of the structures identified with the Q-criterion are on the edges of buildings, particularly the edges of tall buildings that are directly hit by the incoming streamwise flow and

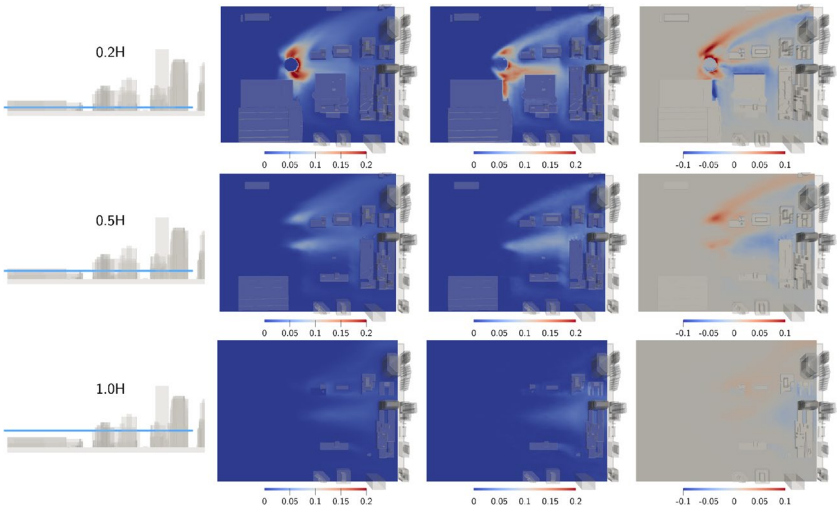

Fig. 11 Comparison of time-averaged contaminant volume fraction for LES (**b**) and MRI (**c**) and the difference between them (**d**). Results are organized by rows that vary the non-dimensional height of the cut plane. The height associated with each row is shown by the plane in the left column (**a**)

have the largest vortices (green arrow in image). Furthermore, the flow within some street canyons generates a strong vortex, particularly the long but narrow spanwise street canyons that have the strongest vortices (red arrow in image). The locations and sizes of the vortices identified with the Q-criterion are very similar between the LES and the MRI results with slightly smaller vortices identified by the LES near the ground and at the roof level.

3.2 Time-averaged contaminant

The time-averaged contaminant volume fraction is shown in Fig. 11. This quantity can also be described as the dose of contaminant observed at each location. High concentrations are observed, as expected, at the lower elevations, close to the contaminant injector in both the LES and MRI measurements. Downstream, both high and low concentrations are observed due to the presence of the buildings. For example, a high concentration of the contaminant is found in the wake of the low building next to the injector ($+z$-direction). Contrarily, a low contaminant concentration is found in spanwise street canyons where there is a large negative vertical velocity that moves clean (uncontaminated) fluid from high in the urban environment into the low region. These noteworthy characteristics are observed in both the LES and MRI results. The difference in the LES predictions and MRI measurements are shown in column (d). The LES consistently overpredicts the rate of dispersion of the contaminant as indicated by higher concentrations on the edges of the plume (red colors in column (d)) and lower concentrations in the middle of the plume (blue colors in column (d)).

To quantify the similarity or difference between the LES prediction and MRI measurements statistical performance measures [61] were computed and shown in Table 1. The table provides the ideal values based on a perfect LES prediction of the MRI observations

Table 1 Statistical performance measures [61] between the MRI concentration observations (C_o) and LES predictions (C_p). In the definitions, the bar $\bar{\cdot}$ indicates spatial average and σ_C indicates standard deviation

Name	Definition	Ideal	Computed
Fractional bias	$\mathrm{FB} = \frac{\overline{C_o} - \overline{C_p}}{0.5(\overline{C_o} - \overline{C_p})}$	0.0	0.02
Geometric mean bias	$\mathrm{MG} = \exp(\overline{\mathrm{In}(C_o)} - \overline{\mathrm{In}(C_p)})$	1.0	1.08
Norm. mean square error	$\mathrm{NMSE} = \frac{\overline{(C_o - C_p)^2}}{\overline{C_o}\,\overline{C_p}}$	0.0	0.23
Geometric variance	$\mathrm{VG} = \exp[\overline{\mathrm{In}(C_o) - \mathrm{In}(C_p)}]$	1.0	1.07
Correlation coefficient	$\mathrm{R} = \frac{\overline{(C_o - \overline{C_o})(C_p - \overline{C_p})}}{\sigma C_o \sigma C_p}$	1.0	0.87
Within factor of two	$\mathrm{FAC2} = \text{fraction in } 0.5 \le \frac{C_p}{C_o} \le 2$	1.0	0.98

and the value computed from the actual simulation and measurements. Note that many of the statistics are only well defined where the contaminant is non-zero, therefore only locations where the minimum LES and MRI concentration is greater than 0.1 are used to compute the statistics. Many of the computed statistics are very close to the value from an ideal model indicating the predictions are statistically similar. The normalized mean square error and correlation coefficient statistics have the largest discrepancies.

3.3 Pulsed contaminant results

The MRI measurements provide the contaminant concentration at twelve times within each period of the pulsed contaminant injection. The LES results were also averaged over multiple periods for comparison with the MRI measurements. Figure 12 shows an isosurface of the contaminant concentration at different times. The first column shows the time and where this time is within the injection pulse (see Fig. 4). The isosurfaces are colored by vertical position or height. At time = 0.12 s, a small amount of contaminant is visible near the injector as well as a larger cloud downstream of the injector from the previous pulse. At time = 0.46 s the injection has created a region of high concentration near the injector at heights near 20 mm (1.0H). Furthermore, at time = 0.46 s, the remnants from the previous injection have mostly moved out of the domain or dissipated below a concentration of 5%. The newly injected contaminant cloud moves downstream with the flow and disperses as shown by the results at time = 0.79 s. Also, visible at this time are interactions of the contaminant cloud with the buildings. The LES and MRI results both capture these important characteristics but the LES overpredicts the rate of dispersion causing the isosurfaces to be smaller than those observed from the MRI measurements.

3.4 Cloud identification algorithm

A significant limitation of the results presented so far is that the contaminant cloud from one injection period is still within the measurement region when the next injection begins. For example, in Fig. 12 at time = 0.12 s a large amount of remnant contaminant from the previous injection is present. One method to avoid this is to lengthen the period of

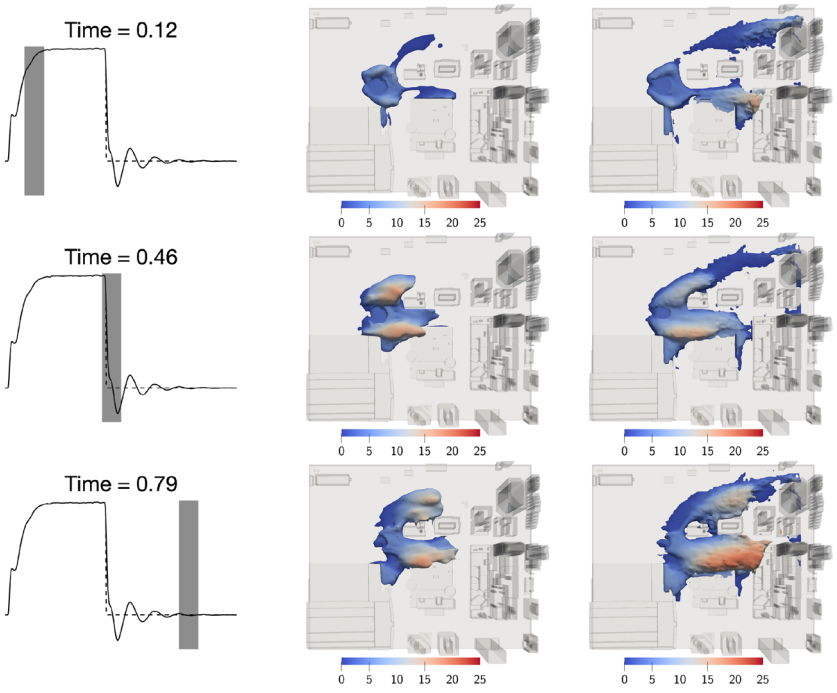

Fig. 12 Comparison of 5% isosurface of contaminant colored by vertical position (mm) for LES (center column) and MRI (right column). Results are organized by rows that vary in time. The time associated with each row is shown in the left column, which shows the time with-respect-to contaminant injection phases

the injection pulses allowing additional time for the contaminant to leave the measurement domain. Here we present an alternative approach, which tries to identify when the contaminant from one injection event ends and the contaminant from the next injection event begins using a post-processing algorithm, which we refer to as the Cloud Identification Algorithm (CIA). This algorithm allows for the calculation of ensemble averages of the time varying results. With these averages, contaminant arrival and residence times are computed, which are two important quantities for determining when a contaminant will arrive at a location and how long the contaminant will remain at that location.

CIA is based on the following principles. At a given location, when a contaminant cloud is leaving the contaminant concentration will decrease. When the contaminant cloud from the next injection arrives at this location, the concentration will start to increase. Therefore, the time when the contaminant concentration is at a minimum can be used as a boundary between the two clouds. Alternatively, at a given time the boundaries of a contaminant cloud are comprised of the band of cells that are currently at their minimum concentration. This latter description is used to construct an algorithm that identifies all the cells within a given cloud at each phase within the injection period. At some cell locations, the interval between clouds consists of more than a single measurement time (i.e., the time interval associated with the minimum concentration value does not represent the entire break between clouds). To account for this, the requirement for cells to represent boundaries

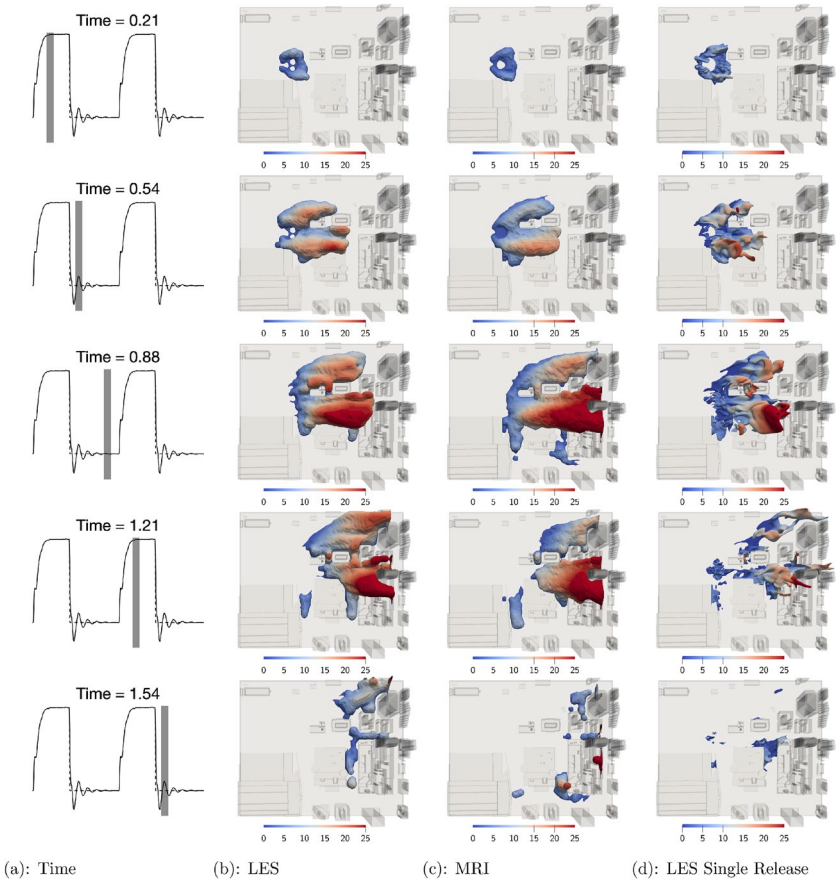

Fig. 13 Comparison of isosurfaces of contaminant identified with the Cloud Identification Algorithm for LES (column b) and MRI (column c). Results are organized by rows that vary in time. The time associated with each row is shown in the left column, which shows the time with-respect-to contaminant injection phases. The results in column d are from an additional LES simulation that had a single release of contaminant

between clouds is relaxed to include cells within 5% of their minima, which is comparable to other works that used a similar approach [62].

Note that once the cells comprising the boundary between clouds are identified using the minimum concentration criteria described above, an image opening and closing operation is used to eliminate any small disconnected regions and holes in the boundary. These disconnections happen when fluctuations in the data cause minima to occur outside of the cloud boundaries (this is especially common in areas of low concentration or high residence). Particularly, the Matlab function bwareaopen is used to remove any detected clouds that are smaller than a 3x3x3 cube of cells and is not connected by a face to another cloud. Next, the Matlab function imclose is used to close any holes in the cloud that are smaller than a sphere with a radius of three cells.

Figure 13 shows the contaminant cloud identified using this algorithm at different times throughout the injection period. Note that since the algorithm allows for tracking the contaminant cloud until it leaves the domain the time is shown over two injection periods.

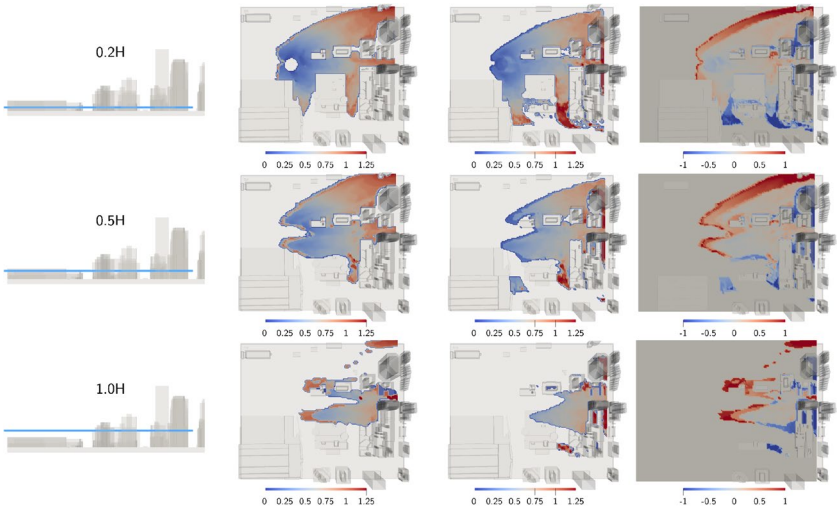

Fig. 14 Comparison of cloud arrival time (s) for for LES (**b**) and MRI (**c**) and the difference between them (**d**). Results are organized by rows that vary the non-dimensional height of the cut plane. The height associated with each row is shown by the plane in the left column (**a**)

With these results it is much easier to see (1) the growth of the contaminant cloud during the injection (time = 0.21–0.54), (2) the advection downstream and dispersion of the cloud, and (3) how the buildings can obstruct the advection and cause contaminant to remain in street canyons. The LES and MRI results agree reasonably well even at later times when the location of the contaminant around the buildings is very similar.

In addition to the time-averaged LES and MRI results, Fig. 13 shows results from an LES simulation that tries to mimic the dynamics of a contaminant cloud being injected and moving through the domain. The simulation consists of a single injection event after which the contaminant injector is turned off. This allows the contaminant from a single release to be tracked through the domain, which is what CIA is attempting to capture. The key downside of this simulation is that it is a single event and thus not averaged over multiple releases. However, the results do show very similar spatial distributions of contaminant when compared to the clouds, albeit noisier due to the lack of averaging. Overall, these results help confirm the usefulness and accuracy of CIA.

CIA allows for contaminant arrival and residence times to be computed. The arrival time is the amount of time between the beginning of the injection event and the arrival of the contaminant cloud at a location, where the arrival time is defined as the time at which a given location has experienced 10% of the total dosage from the cloud as it passes through [62]. Figure 14 shows the arrival time for the LES and MRI on planes at different heights. The arrival time is not defined and is transparent in locations where the cloud does not reach or is always present. At the lowest height ($0.2H$) the arrival time starts at zero at the contaminant injector and increases radially outward. The wakes behind buildings tend to have higher arrival times. Comparing the LES and MRI arrival times shows that both are quite similar, but the arrival times are slightly higher in the far downstream locations in the LES simulation.

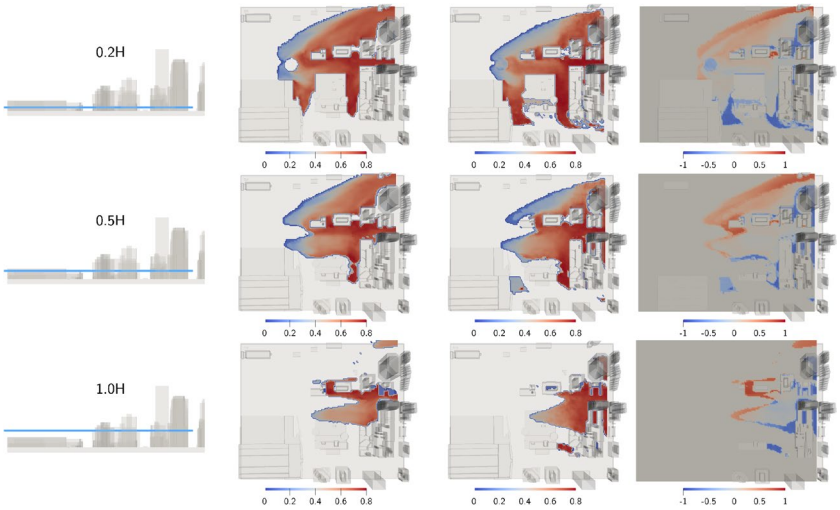

Fig. 15 Comparison of cloud residence time (s) for for LES (**b**) and MRI (**c**) and the difference between them (**d**). Results are organized by rows that vary the non-dimensional height of the cut plane. The height associated with each row is shown by the plane in the left column (**a**)

The residence time is the amount of time between when a contaminant cloud reaches a location to when the cloud leaves the location. The cloud arrival time in this calculation is defined using the same 10% dosage threshold described in the preceding paragraph while leaving time is defined by an analogous 90% dosage threshold. Figure 15 shows the residence time for the LES and MRI measurements at different heights. At all heights, but particularly lower heights, the residence time is largest in street canyons where the contaminant can get trapped and last for a long time. Due to the difference in contaminant dispersion the edges of the residence time plots are large. Where the plumes overlap, the residence time is well-defined and very similar residence times are found with only a slightly larger value in the LES. The difference is likely due to plumes with larger spatial extents due to the higher dispersion in the LES, which results in more time for the plumes to traverse a given location.

4 Conclusions

This work produced LES datasets of the turbulent flow through Oklahoma City as it was in 2003 at a 1:2200 geometric scaling. The flow has a Reynolds number based on the a representative building height of 6000, which provides an approximation of the atmospheric flow and captures the large eddies responsible for contaminant dispersion. The LES results are compared with 4D MRI measurements that were obtained in a three-dimensional field consisting of nearly 2 million measurement voxels across each of 12 discrete time windows during a period when an injection valve opened and closed releasing a contaminant into the flow through the street surface.

Comparisons are provided of streamwise velocity components for the time averaged results as well as the individual time windows across the injection cycle that agree well and

highlight the complex 3D nature of the flow around the buildings. Flow is accelerated several times the bulk averaged velocity through street canyons and develops strong vertical velocities in spanwise street canyons. Differences in time averaged streamwise velocity are most pronounced near surface levels. Vertical velocities near large buildings are of similar magnitude to the averaged streamwise velocity component indicating how significantly these features impact the field, inclusive of both positive and negative components.

The contaminant comparisons show a generally overpredicted concentration in the LES results in part due to the subtle differences in the velocity field and due to increased dispersion rate predictions, suggesting that a matched velocity field is a critical prerequisite for detailed scalar concentration comparisons. Isosurfaces of Q-criterion highlight that in addition to large vortices developing on the edges of buildings, the vortices in some spanwise street canyons can be of similar magnitude suggestive of transport mechanisms in a crosswind direction. Comparisons of contaminant concentrations show similar spatial distributions and temporal dynamics, albeit the LES predicts the contaminant dissipates faster than shown by the MRI measurements. The strong vertical velocities identified previously lead to more dramatic variations in contaminant concentrations than in velocity comparisons.

Statistical performance measures [51] were computed and quantify the agreement between the LES predictions and MRI measurements in a pointwise fashion and overall perform very well but suggest that new comparative metrics could be developed that better leverage the volumetric nature of the data and distinguish between performance of the simulation near complex features where there are important differences.

A novel Cloud Identification Algorithm is proposed and tested. The algorithm separates pulsed injections, identifying unique releases of contaminant. The clouds identified in the LES and MRI results compare very well and the arrival and residence times of clouds are computed and compared which depend strongly on location and height. The clouds identified in the LES and MRI results are compared in contour plots at three vertical planes indicating plume arrival time differences that are spatially varying between the computational and experimental results. A separate simulation consisting of a single release is also compared with the MRI results and suggests that the cloud identification algorithm developed herein is working correctly to separate regions between release events that might still have remnants from earlier plumes from the next injection cycle activity.

This work provides a comparison of lab-scale experiments and corresponding LES simulations with the same geometry and boundary conditions of time varying flow. The demonstrated agreement of the two datasets builds confidence in both techniques for studying the flow of a contaminant in a complex urban environment.

Acknowledgements • Computational efforts were performed on the Hyalite High Performance Computing System, operated and supported by University Information Technology Research Cyberinfrastructure at Montana State University. • Visualizations were created using Paraview [63].

Funding For this work was provided by the United States Defense Threat Reduction Agency under agreement number HDTRA1137491. This material is declared a work of the U.S. Government and is not subject to copyright protection in the United States. Approved for public release; distribution is unlimited.

Declarations

Conflict of interest The authors declare that no Conflict of interest or Conflict of interest exists in the publication of this work. All authors contributed to the study conception and design. Experimental data collection and analysis were performed by Ty Homan, Andrew Banko, and Michael Benson. Simulations were conducted by Mark Owkes. The comparison of the experimental and simulation results was performed by Ty Homan and Mark Owkes. The first draft of the manuscript was written by Mark Owkes and all authors commented on previous versions of the manuscript. All authors read and approved the final manuscript.

References

1. Britter RE, Hanna SR (2003) Flow and dispersion in urban areas. Ann Rev Fluid Mech 35:469–496. https://doi.org/10.1146/annurev.fluid.35.101101.161147
2. Settles GS (2006) Fluid mechanics and homeland security. Annu Rev Fluid Mech 38:87–110
3. Dauxois T et al (2021) Confronting grand challenges in environmental fluid mechanics. Phys Rev Fluids 6:020501
4. Gousseau P, Blocken B, Stathopoulos T, van Heijst GJF (2011) CFD simulation of near-field pollutant dispersion on a high-resolution grid: a case study by LES and RANS for a building group in downtown Montreal. Atmos Environ 45:428–438
5. Nosek Š, Fuka V, Kukačka L, Kluková Z, Jaňour Z (2018) Street-canyon pollution with respect to urban-array complexity: the role of lateral and mean pollution fluxes. Build Environ 138:221–234
6. Akinlabi E, Maronga B, Giometto MG, Li D (2022) Dispersive fluxes within and over a real urban canopy: a large-eddy simulation study. Bound-Layer Meteorol 185:93–128
7. Brown MJ (2004) Urban dispersion-challenges for fast response modeling. Los Alamos Natl. Lab. Rep. LA-UR-04 **5129**
8. Belcher SE (2005) Mixing and transport in urban areas. Philos Trans Royal Soc A: Math, Phys Eng Sci 363:2947–2968
9. Carpentieri M, Hayden P, Robins AG (2012) Wind tunnel measurements of pollutant turbulent fluxes in urban intersections. Atmos Environ 46:669–674
10. Hertwig D et al (2018) Evaluation of fast atmospheric dispersion models in a regular street network. Environ Fluid Mech 18:1007–1044
11. Shim G, Prasad D, Elkins CJ, Eaton JK, Benson MJ (2019) 3D MRI measurements of the effects of wind direction on flow characteristics and contaminant dispersion in a model urban canopy. Environ Fluid Mech 19:851–878. https://doi.org/10.1007/s10652-019-09676-y
12. Lu Y, Zhou X-H, Xiao H, Li Q (2023) Using machine learning to predict urban canopy flows for land surface modeling. Geophys Res Lett 50:e2022GL102313
13. Hertwig D et al (2018) Evaluation of fast atmospheric dispersion models in a regular street network. Environ Fluid Mech 18:1007–1044
14. Singh B, Hansen BS, Brown MJ, Pardyjak ER (2008) Evaluation of the QUIC-URB fast response urban wind model for a cubical building array and wide building street canyon. Environ Fluid Mech 8:281–312
15. Hanna S et al (2011) Comparisons of ju2003 observations with four diagnostic urban wind flow and Lagrangian particle dispersion models. Atmos Environ 45:4073–4081
16. Hernández-Ceballos MA et al (2019) UDINEE: evaluation of multiple models with data from the ju2003 puff releases in Oklahoma city. Part I: comparison of observed and predicted concentrations. Bound-Layer Meteorol 171:323–349
17. García-Sánchez C, van Beeck J, Gorlé C (2018) Predictive large eddy simulations for urban flows: challenges and opportunities. Build Environ 139:146–156
18. Brown AL, Clemenson MD, Benson M, Elkins C, Jones ST (2021) An urban dispersion inspired scenario for CFD model validation. Fire Saf J 120:103130
19. Gousseau P, Blocken B, Stathopoulos T, van Heijst GF (2015) Near-field pollutant dispersion in an actual urban area: analysis of the mass transport mechanism by high-resolution large eddy simulations. Comput & Fluids 114:151–162
20. Letzel MO, Krane M, Raasch S (2008) High resolution urban large-eddy simulation studies from street canyon to neighbourhood scale. Atmos Environ 42:8770–8784
21. Cai X-M, Barlow J, Belcher S (2008) Dispersion and transfer of passive scalars in and above street canyons-large-eddy simulations. Atmos Environ 42:5885–5895

22. Llaguno-Munitxa M, Bou-Zeid E, Hultmark M (2017) The influence of building geometry on street canyon air flow: validation of large eddy simulations against wind tunnel experiments. J Wind Eng Ind Aerodyn 165:115–130
23. Allwine KJ, Flaherty JE (2006) Joint urban 2003: Study overview and instrument locations. Tech. Rep., Pacific Northwest National Lab.(PNNL), Richland
24. Kurppa M et al (2018) Ventilation and air quality in city blocks using large-eddy simulation-urban planning perspective. Atmosphere 9:65
25. Akinlabi EO, Giometto M, Li D (2023) Budgets of second-order turbulence moments over a real urban canopy. Bound-Layer Meteorol 188:351–387
26. Nagel T, Schoetter R, Bourgin V, Masson V, Onofri E (2023) Drag coefficient and turbulence mixing length of local climate zone-based urban morphologies derived using obstacle-resolving modelling. Bound-Layer Meteorol 186:737–769
27. Tian G, Ma Y, Chen Y, Wan M, Chen S (2024) Impact of urban canopy characteristics on turbulence dynamics: insights from large eddy simulation. Build Environ 250:111183
28. Philips D, Rossi R, Iaccarino G (2013) Large-eddy simulation of passive scalar dispersion in an urban-like canopy. J Fluid Mech 723:404–428
29. Cheng W-C, Porté-Agel F (2015) Adjustment of turbulent boundary-layer flow to idealized urban surfaces: a large-eddy simulation study. Bound-Layer Meteorol 155:249–270
30. Cheng W-C, Yang Y (2023) Scaling of flows over realistic urban geometries: a large-eddy simulation study. Bound-Layer Meteorol 186:125–144
31. Wiersema DJ, Lundquist KA, Mirocha JD, Katopodes Chow F (2022) Evaluation of turbulence and dispersion in multiscale atmospheric simulations over complex urban terrain during the joint urban 2003 field campaign. Month Weather Rev 150:3195–3209
32. Li Q, Bou-Zeid E, Anderson W, Grimmond S, Hultmark M (2016) Quality and reliability of les of convective scalar transfer at high Reynolds numbers. Int J Heat Mass Transf 102:959–970
33. Wangsawijaya DD, Nicolai C, Ganapathisubramani B (2022) Time-averaged velocity and scalar fields of the flow over and around a group of cylinders: a model experiment for canopy flows. Flow 2:E9
34. Lim H et al (2022) Pollutant dispersion by tall buildings: laboratory experiments and large-eddy simulation. Exp Fluids 63:92
35. Higson H, Griffiths R, Jones C, Hall D (1994) Concentration measurements around an isolated building: a comparison between wind tunnel and field data. Atmos Environ 28:1827–1836
36. Klein P, Leitl B, Schatzmann M (2011) Concentration fluctuations in a downtown urban area. Part II: analysis of joint urban 2003 wind-tunnel measurements. Environ Fluid Mech 11:43–60
37. Homan TA et al (2021) Magnetic resonance imaging measurements of scalar dispersion for a scaled urban transient release. Build Environ 205:108163
38. Allwine KJ & Flaherty JE (2006) Joint Urban 2003: Study Overview And Instrument Locations. Tech. Rep. PNNL-15967, Pacific Northwest National Lab. (PNNL), Richland, WA (United States). https://www.osti.gov/biblio/890732
39. Klein PM, Young DT (2011) Concentration fluctuations in a downtown urban area Part I: analysis of joint urban 2003 full-scale fast-response measurements. Environ Fluid Mech 11:23–42
40. Klein P, Leitl B, Schatzmann M (2011) Concentration fluctuations in a downtown urban area. Part II: analysis of joint urban 2003 wind-tunnel measurements. Environ Fluid Mech 11:43–60
41. Benson M et al. (2020) Three-Dimensional Concentration and Velocity Measurements of a Pulsatile Contaminant Release in a Model of Oklahoma City. American Society of Mechanical Engineers **10: Fluids Engineering**, V010T10A010
42. Neophytou M, Gowardhan A, Brown M (2011) An inter-comparison of three urban wind models using Oklahoma City Joint Urban 2003 wind field measurements. J Wind Eng Ind Aerodyn 99:357–368
43. Owkes M, Benson M, Elkins C, Wilde N, Van Poppel B (2020) Three-dimensional velocity and concentration measurements and simulations of a scaled Jack Rabbit II mock urban array. Atmos Environ 233:117520
44. Wang L, Shi F, Wang Z, Liang S (2022) Blockage effects in wind tunnel tests for tall buildings with surrounding buildings. Appl Sci 12:7087
45. Robinson M, Klimenko V, Diao Q, Bieringer P, & Annunzio A (2020) Validation of Simulated Urban Microscale Weather Pertinent to Aviation Interests. AIAA AVIATION 2020 FORUM
46. Schultz M, Flack K (2007) The rough-wall turbulent boundary layer from the hydraulically smooth to the fully rough regime. J Fluid Mech 580:381–405
47. Snyder WH, Castro IP (2002) The critical Reynolds number for rough-wall boundary layers. J Wind Eng Ind Aerodyn 90:41–54

48. Huq P, Franzese P (2013) Measurements of turbulence and dispersion in three idealized urban canopies with different aspect ratios and comparisons with a Gaussian Plume model. Bound-Layer Meteorol 147:103–121
49. Snyder WH (1972) Similarity criteria for the application of fluid models to the study of air pollution meteorology. Bound-Layer Meteorol 3:113–134
50. Chew LW, Aliabadi AA, Norford LK (2018) Flows across high aspect ratio street canyons: Reynolds number independence revisited. Environ Fluid Mech 18:1275–1291
51. Castro I, Robins A (1977) The flow around a surface-mounted cube in uniform and turbulent streams. J Fluid Mech 79:307–335
52. Snyder WH (1981) Guideline for fluid modeling of atmospheric diffusion, vol 81. Environmental Sciences Research Laboratory, Office of Research and ...
53. Hearst RJ, Gomit G, Ganapathisubramani B (2016) Effect of turbulence on the wake of a wall-mounted cube. J Fluid Mech 804:513–530
54. Markl M et al (2003) Time-resolved three-dimensional phase-contrast MRI. J Magn Reson Imag: JMRI 17:499–506
55. Banko AJ, Benson MJ, Gunady IE, Elkins CJ, Eaton JK (2020) An improved three-dimensional concentration measurement technique using magnetic resonance imaging. Exp Fluids 61:53. https://doi.org/10.1007/s00348-020-2889-9
56. Elkins CJ, Alley MT (2007) Magnetic resonance velocimetry: applications of magnetic resonance imaging in the measurement of fluid motion. Exp Fluids 43:823–858. https://doi.org/10.1007/s00348-007-0383-2
57. Benson MJ, Elkins CJ, Mobley PD, Alley MT, Eaton JK (2010) Three-dimensional concentration field measurements in a mixing layer using magnetic resonance imaging. Exp Fluids 49:43–55. https://doi.org/10.1007/s00348-009-0763-x
58. Tominaga Y, Stathopoulos T (2013) CFD simulation of near-field pollutant dispersion in the urban environment: a review of current modeling techniques. Atmos Environ 79:716–730
59. Lateb M et al (2016) On the use of numerical modelling for near-field pollutant dispersion in urban environments - A review. Environ Pollut 208:271–283
60. Jeong J, Hussain F (1995) On the identification of a vortex. J Fluid Mech 285:69–94
61. Chang JC, Hanna SR (2004) Air quality model performance evaluation. Meteorol Atmos Phys 87:167–196. https://doi.org/10.1007/s00703-003-0070-7
62. Efthimiou GC, Andronopoulos S, Bartzis JG (2018) Prediction of dosage-based parameters from the puff dispersion of airborne materials in urban environments using the CFD-RANS methodology. Meteorol Atmos Phys 130:107–124. https://doi.org/10.1007/s00703-017-0506-0
63. Ahrens, J., Geveci, B. & Law, C. Visualization Handbook, Ch. ParaView: An End-User Tool for Large Data Visualization, 717–731 (Elsevier Inc., Burlington, MA, USA, 2005). https://www.sciencedirect.com/book/9780123875822/visualization-handbook